The Astrophysical Journal, 976:218 (14pp), 2024 December 1 https://doi.org/10.3847/1538-4357/ad863b

JWST Resolves Collision-induced Absorption Features in White Dwarfs

Simon Blouin[1], Mukremin Kilic[2], Loïc Albert[3,4], Bianca Azartash-Namin[2], and Patrick Dufour[3,4]
[1] Department of Physics and Astronomy, University of Victoria, Victoria, BC V8W 2Y2, Canada
[2] Homer L. Dodge Department of Physics and Astronomy, University of Oklahoma, Norman, OK 73019, USA
[3] Département de Physique, Université de Montréal, Montréal, QC H3C 3J7, Canada
[4] Institut Trottier de Recherche sur les exoplanètes, Université de Montréal, Montréal, QC H3C 3J7, Canada
Received 2024 September 7; revised 2024 October 11; accepted 2024 October 11; published 2024 November 25

Abstract

Infrared-faint white dwarfs are cool white dwarfs exhibiting significant infrared flux deficits, most often attributed to collision-induced absorption (CIA) from H_2–He in mixed hydrogen–helium atmospheres. We present James Webb Space Telescope (JWST) near- and mid-infrared spectra of three such objects using Near-Infrared Spectrograph (0.6–5.3 μm) and Mid-Infrared Instrument (5–14 μm): LHS 3250, WD J1922+0233, and LHS 1126. Surprisingly, for LHS 3250, we detect no H_2–He CIA absorption at 2.4 μm, instead observing an unexpected small flux bump at this wavelength. WD J1922 +0233 exhibits the anticipated strong absorption feature centered at 2.4 μm, but with an unexpected narrow emission-like feature inside this absorption band. LHS 1126 shows no CIA features and follows a λ^{-2} power law in the mid-infrared. LHS 1126's lack of CIA features suggests a very low hydrogen abundance, with its infrared flux depletion likely caused by He–He–He CIA. For LHS 3250 and WD J1922+0233, the absence of a 1.2 μm CIA feature in both stars argues against ultracool temperatures, supporting recent suggestions that infrared-faint (IR-faint) white dwarfs are warmer and more massive than previously thought. This conclusion is further solidified by Keck near-infrared spectroscopy of seven additional objects. We explore possible explanations for the unexpected emission-like features in both stars, and temperature inversions above the photosphere emerge as a promising hypothesis. Such inversions may be common among the IR-faint population, and since they significantly affect the infrared spectral energy distribution, this would impact their photometric fits. Further JWST observations are needed to confirm the prevalence of this phenomenon and guide the development of improved atmospheric models.

Unified Astronomy Thesaurus concepts: Infrared spectroscopy (2285); Stellar atmospheres (1584); Stellar atmospheric opacity (1585); White dwarf stars (1799)

1. Introduction

The atmosphere of a white dwarf becomes increasingly transparent as it ages and cools. As a result, the photosphere is located progressively deeper into the star and can reach liquid-like densities of a few grams per cubic centimeter in the most extreme cases (i.e., a hydrogen-deficient atmosphere at an effective temperature of less than ≃4000 K; D. Saumon et al. 2022). These conditions are unusual for stellar atmospheres, where ideal-gas conditions usually prevail (e.g., $\rho \sim 10^{-7}$ g cm^{-3} at the photosphere of the Sun). In cool white dwarf atmospheres ($T_{\rm eff} \lesssim 6000$ K), interactions between species affect the equation of state and the opacity of the gas. Modeling these nonideal effects is challenging, but the increasing availability of quantum chemistry simulation codes and supercomputing resources has allowed significant progress (e.g., P. M. Kowalski et al. 2007; P. M. Kowalski 2010; S. Blouin et al. 2017, 2018a). These advances have in turn led to a qualitative improvement in the quality of spectroscopic fits to the absorption features of cool white dwarfs (S. Blouin et al. 2019a, 2019b; S. Blouin & P. Dufour 2019).

However, this progress still stops short of explaining the peculiar spectral energy distributions (SEDs) of infrared-faint (IR-faint) white dwarfs.[5] These objects suffer from significant absorption in the infrared (peaking at 2.4 μm), which results in surprisingly blue colors for their low temperatures ($T_{\rm eff} \lesssim 5000$ K). This infrared absorption is attributed to collision-induced absorption (CIA) from H_2–X complexes in their mixed hydrogen–helium atmospheres (B. M. S. Hansen 1998; U. G. Jørgensen et al. 2000; P. Bergeron & S. K. Leggett 2002; A. Gianninas et al. 2015; P. Bergeron et al. 2022). White dwarfs with pure-hydrogen atmospheres are not thought to significantly contribute to the observed IR-faint population, because CIA becomes dominant only at extremely low temperatures in those stars ($T_{\rm eff} \lesssim 4000$ K) due to their lower photospheric densities (see Figure 16 of D. Saumon et al. 2022). Given the finite age of the Galactic disk, there are few white dwarfs that have had enough time to cool to such low temperatures. Similarly, white dwarfs with pure (or nearly pure) helium atmospheres lack the molecular hydrogen required for strong infrared absorption, although it has been suggested that He–He–He complexes constitute a significant source of CIA in some hydrogen-depleted white dwarfs (P. M. Kowalski 2014).[6]

The existence of a population of cool white dwarfs with mixed hydrogen–helium atmospheres is most likely the result of convective mixing (B. Rolland et al. 2018; A. Bédard et al. 2022; P. Bergeron et al. 2022). As a white dwarf cools down, the superficial hydrogen convection zone deepens. If the hydrogen layer is thin enough ($M_{\rm H}/M_\star \lesssim 10^{-6}$), the bottom of this convection zone eventually reaches the much thicker

[5] IR-faint white dwarfs are often referred to as ultracool white dwarfs in the literature. However, P. Bergeron et al. (2022) suggest abandoning this term following their findings that these stars might not be so cool after all. We adhere to this convention in this work.

[6] CIA in a pure-helium medium requires three-body collisions because interactions between two identical atoms are infrared inactive due to the lack of a net induced dipole moment. Three-body collisions break this symmetry, allowing for a temporary dipole moment and thus enabling infrared absorption.

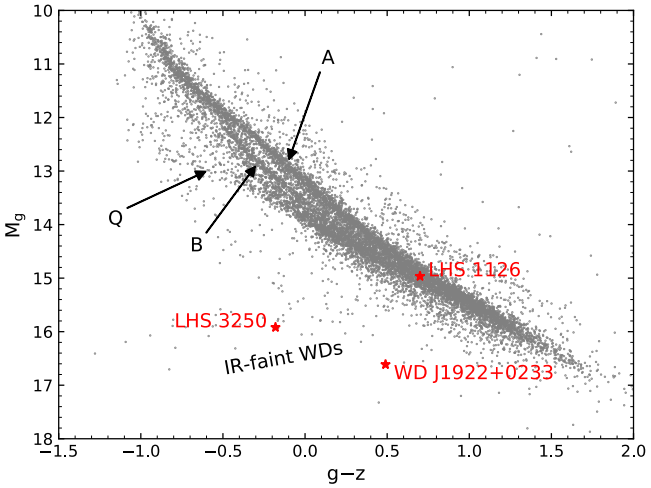

Figure 1. Color–magnitude diagram of the Pan–STARRS white dwarfs within 100 pc of the Sun and with 10σ Gaia DR3 parallax measurements. Labels indicate the location of the A, B, Q, and IR-faint branches. The stars analyzed in this work are shown in red. The IR-faint branch starts at $M_g \simeq 15$, $g - z \simeq 0.5$ and extends toward the bottom-left corner of the figure.

helium layer underneath, thereby transforming a pure-hydrogen-atmosphere into a mixed hydrogen–helium composition. As these convectively mixed objects cool down, they inevitably develop CIA and become infrared faint.

When CIA absorption is particularly intense, it can act beyond the infrared region and also reduce the emerging flux in the red optical (H. C. Harris et al. 1999; E. Gates et al. 2004), creating a distinct IR-faint sequence in the Sloan Digital Sky Survey (M. Kilic et al. 2020) or Pan–STARRS color–magnitude diagram (Figure 1). This sequence likely extends below the $M_g \simeq 16.5$ cutoff visible in Figure 1, which is thought to be the result of Gaia's limiting magnitude (P. Bergeron et al. 2022). While there are now good explanations for the presence of the B and Q branches in this and similar color–magnitude diagrams (P. Bergeron et al. 2019; P.-E. Tremblay et al. 2019; S. Blouin et al. 2021; S. Blouin et al. 2023a, 2023b; M. Camisassa et al. 2023; A. Bédard et al. 2024), the exact origins and the properties of the stars belonging to the IR-faint branch remain uncertain.

To illustrate the extent of current uncertainties, consider the example of WD J192206.20+023313.29 (hereafter WD J1922+0233). This star was independently analyzed by A. K. Elms et al. (2022) and P. Bergeron et al. (2022). Different choices of input physics have led these two teams to converge to widely different atmospheric parameters. A. K. Elms et al. (2022) conclude that WD J1922+0233 has a normal mass and an ultracool temperature ($0.57\,M_\odot$, $T_{\rm eff} = 3340$ K), while P. Bergeron et al. (2022) find a high-mass and not-so-cool solution ($1.07\,M_\odot$, $T_{\rm eff} = 4440$ K). It would be troubling enough to have such a high level of disagreement between two analyses, but equally concerning is that both teams' best solutions actually provide a poor match to the available photometric and spectroscopic data.[7]

Because IR-faint white dwarfs only constitute a small fraction of the known white dwarf population (P. Bergeron et al. 2022 were able to identify 105 IR-faint white dwarfs), it is tempting to ignore these outliers, considering them to be unimportant exceptions. However, we do not have that luxury. The possibility that IR-faint white dwarfs are among the coolest, oldest white dwarfs in our Galaxy makes them particularly interesting targets for age-dating applications. Yet, current uncertainties on their temperatures and masses make this impracticable. For example, there is a $\simeq$2 Gyr cooling age difference between the best-fit solutions of A. K. Elms et al. (2022) and P. Bergeron et al. (2022) for WD J1922+0233. Furthermore, the atmospheres of some IR-faint white dwarfs are contaminated by planetary material (S. Blouin et al. 2018b; M. A. Hollands et al. 2021; B. C. Kaiser et al. 2021; A. K. Elms et al. 2022). This represents a unique window into the formation and evolution of planetary systems that arose during the Milky Way's infancy. Exploiting this opportunity requires reliable model atmospheres to accurately determine the chemical composition of the accreted planetary material.

As alluded to above, P. Bergeron et al. (2022) recently suggested that most IR-faint white dwarfs are not as cool as previously believed. Earlier analyses of IR-faint samples found most IR-faint white dwarfs having $T_{\rm eff} \lesssim 4000$ K, with many even being cooler than 3000 K (A. Gianninas et al. 2015; M. Kilic et al. 2020). There were at least two major reasons for doubting these ultracool temperatures. First, large white dwarf radii were needed to reconcile the observed luminosities with the ultracool temperatures. This led to very small white dwarf masses ($\sim 0.2\,M_\odot$). These can only be produced as the result of evolution in interacting binaries (W. R. Brown et al. 2010), since single-star evolution needs more than a Hubble time to produce such low-mass white dwarfs. The problem is that the existence of a sizeable population of extremely low-mass white dwarfs at ultracool temperatures is incompatible with the scarcity of such objects at higher temperatures (M. Kilic et al. 2020). Second, the agreement between the photometric data and model spectral energy distribution (SED) was very poor for most objects. P. Bergeron et al. (2022) presented new model atmospheres, which include more accurate helium opacities at high densities (C. A. Iglesias et al. 2002; see also P. Kowalski 2006; S. Blouin et al. 2018a). In these models, the increased transparency of helium makes the photosphere denser and H_2–He CIA stronger. This enabled P. Bergeron et al. (2022) to find much warmer solutions (most being in the $4000\ {\rm K} \leqslant T_{\rm eff} \leqslant 5000$ K range) and therefore smaller radii and higher masses. In addition, the quality of the fits improved considerably.

While the analysis of P. Bergeron et al. (2022) apparently solves the two major issues that affected previous analyses of IR-faint samples, it generates new questions. First, the improved fits obtained by P. Bergeron et al. (2022) rely on the H_2–He CIA calculations of U. G. Jørgensen et al. (2000). The more recent calculations of M. Abel et al. (2012) predict a significantly different absorption spectrum for H_2–He CIA, which does not lead to satisfying SED fits. This is perplexing because the M. Abel et al. (2012) CIA spectra are based on more detailed calculations than U. G. Jørgensen et al. (2000) and should a priori be considered more reliable. Second, the best-fit parameters of P. Bergeron et al. (2022) often lead to high-mass solutions ($\sim 1.0\,M_\odot$). The combination of relatively cool temperatures and high masses places these objects in the Debye cooling phase of white dwarf evolution (G. Fontaine et al. 2001). This is surprising because white dwarf cooling proceeds at an accelerated pace in this regime due to the rapidly

[7] At least when ad hoc changes to the models' constitutive physics are not introduced.

falling heat capacity of the crystallized core, and therefore few objects are expected to be found in this phase.

To shed light on this issue and pave the way forward to reliable parameter determinations for these objects, we obtained infrared spectra of three IR-faint white dwarfs using the James Webb Space Telescope (JWST) Near-Infrared Spectrograph (NIRSpec; P. Jakobsen et al. 2022) and Mid-Infrared Instrument (MIRI; G. H. Rieke et al. 2015). For the first time, these observations resolve the CIA features of white dwarfs, providing new observational constraints that can be used to discriminate between models. We describe these observations in Section 2 and the models we use to analyze them in Section 3. Our analysis of the JWST spectra is then presented in Section 4. As we will see, two of our JWST spectra exhibit an unexpected emission-like feature, the origin of which we investigate in Section 5. Section 6 presents Keck near-infrared spectroscopic data for seven additional IR-faint white dwarfs that further support one of the key conclusions drawn from our analysis of the JWST spectra. We finally discuss the implications of our results for our understanding of IR-faint white dwarfs in Section 7 along with our conclusions.

2. JWST Observations

2.1. Choice of Targets

Our observing program (GO-3168, PI: Blouin) targeted three IR-faint white dwarfs: LHS 3250, WD 1922+0233, and LHS 1126. These objects were selected to provide the most useful constraints on IR-faint atmosphere models.

LHS 3250 is the prototypical IR-faint white dwarf (H. C. Harris et al. 1999). As the most studied object of its class, it was natural to include it in our sample. In addition, Spitzer photometry of LHS 3250 showed evidence of a flat or even increasing mid-infrared flux distribution (M. Kilic et al. 2009). This is not predicted by any model atmosphere, and JWST observations were deemed essential to resolve this discrepancy and potentially uncover new physics in IR-faint white dwarf atmospheres.

WD J1922+0233 is a more recent addition to the IR-faint white dwarf catalog (P. E. Tremblay et al. 2020; P. Bergeron et al. 2022; A. K. Elms et al. 2022). It is particularly interesting given the detection of metal lines in its optical spectrum. In theory, these features can provide constraints on the atmospheric density. As we have seen, recent analyses of WD J1922+0233 have led to conflicting results regarding its temperature and mass (P. Bergeron et al. 2022; A. K. Elms et al. 2022), making it an excellent test case for investigating current uncertainties in the modeling of IR-faint white dwarfs.

With an estimated effective temperature of 5200 K (S. Blouin et al. 2019b; P. Bergeron et al. 2022), LHS 1126 is one of the warmest known white dwarfs exhibiting clear signs of CIA in the infrared. LHS 1126 has been observed with Hubble Space Telescope (HST)/Faint Object Spectrograph (FOS; B. Wolff et al. 2002) and Spitzer/IRAC (M. Kilic et al. 2006). No model to date can simultaneously reproduce its entire SED (S. Blouin et al. 2019b). While these discrepancies make LHS 1126 an ideal target for investigating the limitations in our understanding of opacity sources in cool white dwarf atmospheres, it remains unclear whether LHS 1126 is a unique oddity or representative of a broader class of objects. In fact, LHS 1126's optical spectrum also shows weak molecular carbon bands, which is unique among the IR-faint population.

2.2. Observational Setup and Data Reduction

We obtained infrared spectra of our three targets using NIRSpec and MIRI. NIRSpec's low-resolution prism mode ($R \sim 100$) was used for the 0.6–5.3 μm range, while MIRI's Low Resolution Spectrometer ($R \sim 100$) covered 5–14 μm. Low-resolution spectroscopy is sufficient, as the CIA features are intrinsically broad. This setup provides continuous coverage across the entire 0.6–14 μm range, ideal for tracing the overall SED and resolving broad molecular features.

We employed a two-point dither strategy and chose integration times to achieve a signal-to-noise ratio (S/N) $\geqslant$ 50 at 4.5 μm (NIRSpec) and S/N $\geqslant$ 25 at 8.0 μm (MIRI). The total integration times were 0.3 hr for LHS 1126, 2.4 hr for LHS 3250, and 4.7 hr for WD J1922+0233.

The data were reduced with the JWST calibration pipeline version 1.14.0 (H. Bushouse et al. 2022). Both the raw and fully reduced data were retrieved from the Mikulski Archive for Space Telescopes (MAST). These data can be accessed via the doi:10.17909/3sgc-yq02.

The pipeline-extracted NIRSpec prism spectra display a few spurious narrow absorption features. These features are found at different wavelengths in each dither position, and are not intrinsic to the source. We used the NIRSpec optimal spectral extraction notebook, but found no significant differences between the locally reduced data and the extracted data available from MAST. The spurious features are present in the optimally extracted spectra as well. For example, LHS 1126's spectrum shows a narrow dip at 4.72 μm in the first dither position and two narrow dips at 3.98 and 4.97 μm in the second dither position. These spurious features are not unique to our observations. For example, the NIRSpec data of the dusty white dwarf GD 362 obtained as part of the GO program 2919 also displays spurious narrow absorption features at various wavelengths in each dither position. Since our NIRSpec observations were obtained at only two dither positions, these spurious features make it to the final combined spectrum. Going forward, we recommend conducting NIRSpec observations with more than two dither positions (like in the case of GD 362) so that the spurious features can be rejected statistically.

2.3. General Description of the Spectra

The combined NIRSpec and MIRI spectra for our three targets are presented in Figure 2. The two spectra were stitched at 5.0 μm without any adjustment, and they merge seamlessly. For comparison, we also show photometry from other surveys and programs.

WD J1922+0233 exhibits by far the most striking spectrum of the three objects. The spectrum shows a strong absorption feature centered at 2.4 μm, consistent with what we expect for H_2–He CIA (this is the fundamental H_2 vibrational band). Surprisingly, we observe a narrow emission-like feature inside this 2.4 μm absorption band, which is not predicted by any existing model.

Against all expectations and model predictions, LHS 3250 shows no absorption feature at 2.4 μm where CIA is expected to peak. Instead, we observe a small bump at that wavelength, which is not predicted by any current model. While the bump is subtle, it appears to be a real feature of LHS 3250's spectrum; we have no indications to the contrary. Unlike earlier tentative indications from relatively noisy Spitzer photometry (M. Kilic et al. 2009), we do not observe an increasing flux in the mid-infrared for this object.

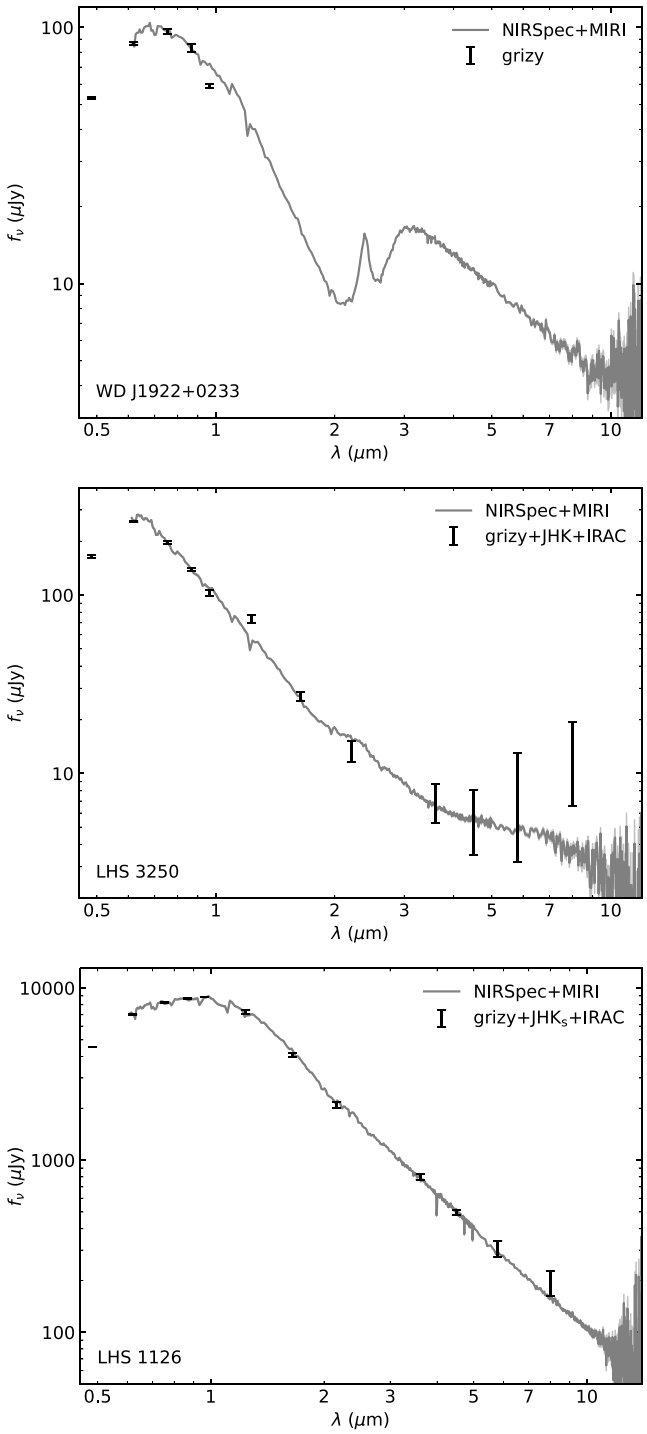

Figure 2. NIRSpec and MIRI spectra of the three IR-faint white dwarfs observed as part of our program. Both spectra are merged at 5 μm. Photometry data from the literature are shown for comparison (H. C. Harris et al. 1999; M. Kilic et al. 2006, 2009; M. F. Skrutskie et al. 2006; K. C. Chambers et al. 2016).

The mid-infrared spectrum of LHS 1126 follows a λ^{-2} power law with remarkable precision, consistent with the findings of M. Kilic et al. (2006) based on Spitzer photometry. Notably, similar to LHS 3250, there is no sign of a CIA absorption feature at 2.4 μm, despite both H_2–H_2 and H_2–He CIA peaking at that wavelength.

The fact that both WD J1922+0233 and LHS 3250 exhibit unexpected emission-like features at similar wavelengths is intriguing and suggests a possible common origin for these

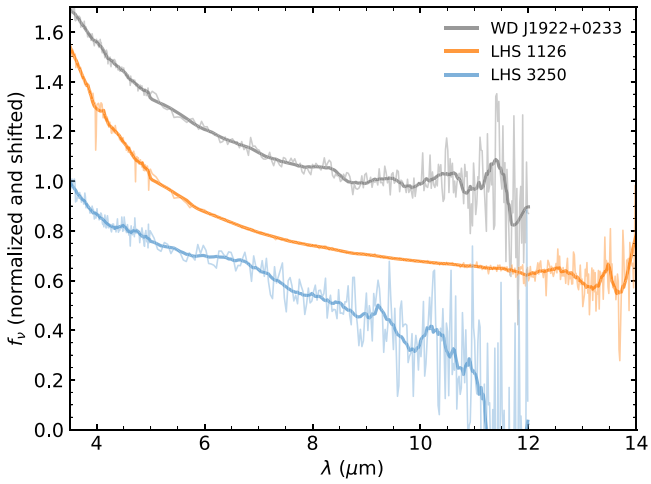

Figure 3. JWST MIRI spectra of the three IR-faint white dwarfs in our sample, focused on the 3.5–14 μm region. The spectra are normalized at 3.5 μm and vertically offset for clarity. Thin lines show the original spectra, while thick lines represent smoothed versions using a Savitzky–Golay filter. No clear silicate emission features are detected in the 8–12 μm range. For WD J1922+0233 and LHS 3250, the spectra are cut off at 12 μm due to poor S/Ns at longer wavelengths.

phenomena. The wavelength of 2.4 μm corresponds to the $\Delta\nu = 1$ vibrational transition of the H_2 molecule. Therefore, there is a strong expectation, based on fundamental molecular physics, that H_2–He CIA is particularly opaque at that wavelength. This is also consistently predicted by all available CIA calculations (J. L. Linsky 1969; A. Borysow et al. 1989; U. G. Jørgensen et al. 2000; M. Abel et al. 2012; S. Blouin et al. 2017). The emission-like features we observe at this wavelength thus represent a significant departure from basic expectations that cannot be easily explained by remaining opacity uncertainties alone. This discrepancy necessitates the exploration of alternative explanations, which will be the focus of Section 5.

Finally, note that we do not detect any clear silicate emission features in the MIRI spectra of our three targets. Figure 3 shows the 8–12 μm region where silicate features have been observed in dusty white dwarfs (W. T. Reach et al. 2005, 2009; M. Jura et al. 2009; J. Farihi 2016; A. Swan et al. 2024). While there are some fluctuations in the spectra, these appear consistent with the noise level of our observations.

3. Model Atmospheres

The model atmosphere calculations in this work are based on the code described in detail in S. Blouin et al. (2018a, 2018b). This code incorporates several physical improvements for modeling cool, high-density white dwarf atmospheres, including a nonideal equation of state (A. Becker et al. 2014), a refined treatment of helium ionization equilibrium following P. M. Kowalski et al. (2007), high-density corrections to helium continuum opacities (C. A. Iglesias et al. 2002), and H_2–He CIA spectra from M. Abel et al. (2012) with high-density corrections from S. Blouin et al. (2017).

We use and expand a model atmosphere grid originally calculated by S. Blouin et al. (2019b). This grid spans effective temperatures of 3750–7000 K in steps of 250 K, surface gravities $\log g = 7.0$–9.0 in steps of 0.5 dex, and hydrogen-to-helium number ratios ranging from pure-helium to pure-hydrogen, with

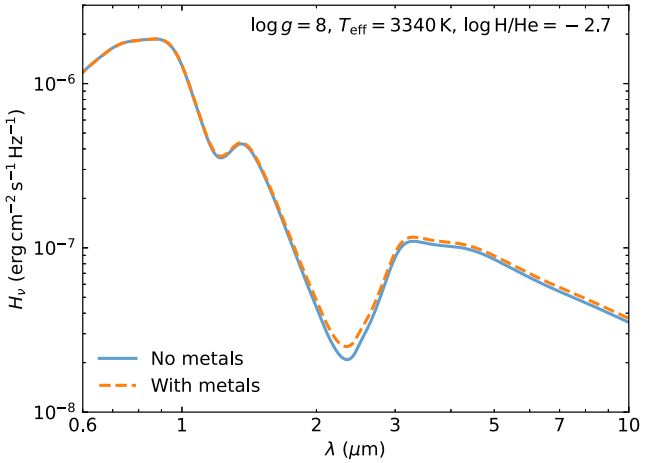

Figure 4. Model spectra for a star with the same parameters as those obtained by A. K. Elms et al. (2022) for WD J1922+0233. The solid line shows a model without metal pollution, while the dashed line corresponds to the case with metals (log Na/He = −12.6 and chondritic metal-to-metal abundance ratios for the other elements).

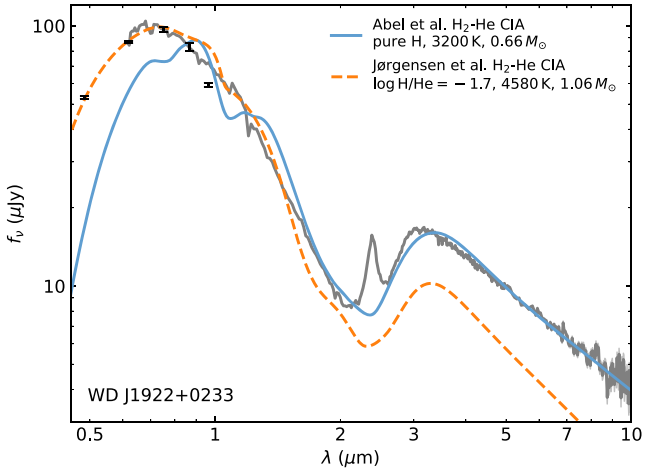

Figure 5. Best-fit models to the JWST spectrum of WD J1922+0233. The solid blue line displays the best fit for a grid of models using the M. Abel et al. (2012) opacities for H_2–He CIA, while the dashed orange line is for a grid of models using the U. G. Jørgensen et al. (2000) H_2–He CIA.

intermediate values of logH/He = −5, −4.5,…, 1.5, 2. We extended the grid to lower temperatures (as cool as 3000 K) and higher surface gravities (up to $\log g = 9.5$).

In addition to this extended grid, we calculated a second set of models based on the findings of P. Bergeron et al. (2022). This second grid is identical to the first in all respects except for the adopted H_2–He CIA opacity. Instead of the M. Abel et al. (2012) CIA spectra, it uses the earlier calculations of U. G. Jørgensen et al. (2000), including the density-dependent correction factor from W. F. J. Hare & H. L. Welsh (1958). This dual-grid approach allows us to assess the impact of different CIA opacities on inferred white dwarf properties and to determine which best fit the JWST spectra.

To analyze the JWST spectroscopy, we employ a fitting procedure similar to the photometric method (P. Bergeron et al. 2001). Since the JWST spectra are well calibrated in flux, we can directly fit $T_{\rm eff}$, the solid angle $\pi(R/D)^2$, and the hydrogen-to-helium ratio to the observed spectrum. This method involves minimizing the χ^2 between the synthetic and observed spectra using the Levenberg–Marquardt algorithm. The solid angle, combined with the distance D obtained from Gaia Data Release 3 (DR3) parallax measurements (Gaia Collaboration et al. 2016, 2023), allows us to determine the radius R of the white dwarf. We use the mass–radius relation from evolutionary models (A. Bédard et al. 2022) to derive the mass and surface gravity of the star from this R, thereby finding a self-consistent set of stellar parameters.

We do not attempt to provide error bars on our fitted parameters. The statistical uncertainties from the fitting procedure are very small and likely negligible compared to the systematic uncertainties stemming from the limitations in our understanding of the physics of these objects. The primary goal of this paper is not to provide precise characterization of individual stars, but rather to gain qualitative insights into the nature of IR-faint white dwarfs.

4. Spectral Fits

4.1. WD J1922+0233

Although WD J1922+0233 is known to be metal polluted, we analyze it using metal-free models. This approach is justified because we expect the impact of metals on the overall SED to be minimal. This is illustrated in Figure 4, where we compare a model with the metal abundance of A. K. Elms et al. (2022) to one without any metals. The difference between both models is insignificant. This aligns with A. K. Elms et al. (2022), who reported that including metals in their fit of WD J1922+0233 altered the synthetic photometry by less than 0.01 mag. Adopting metal-free models significantly reduces the number of atmosphere calculations required, which is particularly advantageous given the convergence difficulties often encountered in this regime of physical parameters (P. Bergeron et al. 1995). These models frequently necessitate time-consuming manual interventions to achieve convergence. Moreover, as we will demonstrate, there are clearly more significant uncertainties in the models, such that the marginal effect of metals on the SED can be safely disregarded in the context of this analysis.

Figure 5 presents the best-fit models for WD J1922+0233 using our two model grids. Neither model reproduces the emission-like feature at 2.4 μm, which is simply not predicted by standard atmosphere models. We will explore possible explanations for this feature in Section 5.

The grid using M. Abel et al. (2012) CIA opacities yields an ultracool solution (3200 K), but, interestingly, it converges on a pure-hydrogen composition. Mixed hydrogen–helium solutions provide worse fits, meaning that the best-fit model shown here actually relies on the H_2–H_2 CIA opacities from A. Borysow et al. (2001) rather than the H_2–He opacities from M. Abel et al. (2012). While this solution provides a reasonable fit to most of the infrared spectrum, it fails dramatically at wavelengths below $\simeq$1.5 μm. The good fit in the infrared comes at the expense of severely underpredicting the flux in the visible region. Moreover, it predicts a strong absorption band at 1.2 μm (the molecular hydrogen first overtone band) that is not observed in the NIRSpec spectrum. This 1.2 μm feature is even more pronounced in the best-fit solution of A. K. Elms et al. (2022, see their Figure 3).

In contrast, the solution obtained using the Jørgensen et al. CIA opacities largely avoids these issues. It provides a good agreement in the optical region, and the 1.2 μm feature is much weaker due to the warmer temperature. While there is an offset

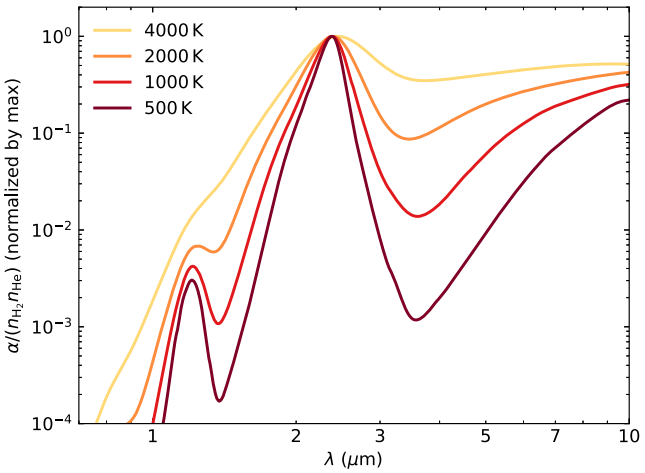

Figure 6. H_2–He CIA spectra at different temperatures from M. Abel et al. (2012). Each absorption spectrum is normalized at its maximum (without this normalization, the higher-temperature spectra would sit above the lower-temperature spectra). Note that the CIA-forming region of the atmosphere is typically much cooler than $T_{\rm eff}$ due to the high opacity at these wavelengths (Figure 13). This results in the emergent flux originating predominantly from the cooler, upper atmospheric layers.

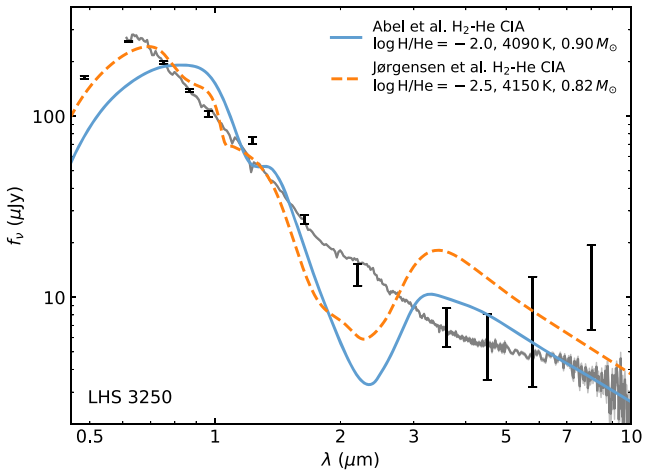

Figure 7. Best-fit models to the JWST spectrum of LHS 3250. The solid blue line displays the best fit for a grid of models using the M. Abel et al. (2012) opacities for H_2–He CIA, while the dashed orange line is for a grid of models using the U. G. Jørgensen et al. (2000) H_2–He CIA.

in the infrared beyond 2 μm, the general shape of the spectrum is well reproduced. We will discuss a possible explanation for this offset in Section 5. Note that this solution (1.06 $M_\odot$, $T_{\rm eff} = 4580$ K) is very similar to that found by P. Bergeron et al. (2022; 1.07 $M_\odot$, $T_{\rm eff} = 4440$ K). This is despite differences in the models' input physics, notably the use of an ideal-gas equation of state in P. Bergeron et al. (2022) and a different treatment of helium pressure ionization.

Overall, our analysis lends additional credence to the claim by P. Bergeron et al. (2022) that IR-faint white dwarfs are not as cool as previously thought. In particular, this conclusion is supported by the absence of a clear 1.2 μm feature in the JWST spectrum. At low temperatures, H_2–He and H_2–H_2 CIA spectra are expected to develop a pronounced and well-defined absorption feature at 1.2 μm (A. Borysow et al. 1997, 2001; U. G. Jørgensen et al. 2000; M. Abel et al. 2012; see also Figure 6) due to reduced thermal broadening and enhanced dimer formation in a low-temperature gas (L. Frommhold 1993). The absence of this feature, which should be particularly distinct if WD J1922+0233 were indeed ultracool, suggests it is not so cool. Of course, we should caution that CIA spectra remain uncertain, but this pronounced 1.2 μm feature is a robust prediction of all available CIA calculations.

4.2. LHS 3250

Figure 7 presents the best-fit models for LHS 3250 using our two model grids. Both solutions fail to reproduce the observed JWST spectrum due to their prediction of a strong H_2–He absorption band at 2.4 μm that is surprisingly absent from the data. However, it is noteworthy that the small bump observed in the JWST spectrum aligns with the peak-CIA absorption in both model fits. This intriguing feature will be further discussed in Section 5.

Despite the poor quality of the fits, both solutions yield similar stellar parameters. The grid using the Abel et al. CIA opacities results in a mass of 0.90 $M_\odot$ and $T_{\rm eff} = 4090$ K, while the U. G. Jørgensen et al. (2000) grid yields 0.82 $M_\odot$ and $T_{\rm eff} = 4150$ K. These temperatures are cooler than the solution

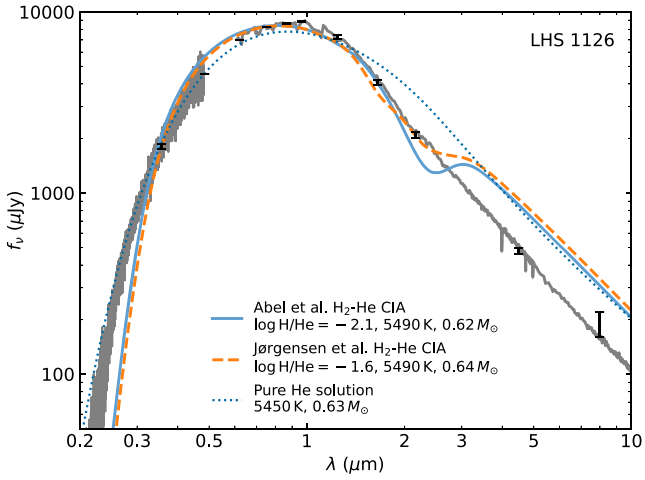

Figure 8. Best-fit models for LHS 1126. The solid blue line displays the best-fit solution to the JWST data for a grid of models using the M. Abel et al. (2012) opacities for H_2–He CIA, while the dashed orange line is for a grid of models using the U. G. Jørgensen et al. (2000) H_2–He CIA. Also shown as a dotted dark blue line is the best-fit solution to the combined HST and JWST SED assuming a pure-helium-atmosphere.

found by P. Bergeron et al. (2022; 1.05 $M_\odot$, $T_{\rm eff} = 4990$ K), but significantly warmer than earlier ultracool, low-mass solutions such as those of P. Bergeron & S. K. Leggett (2002; 0.23 $M_\odot$, $T_{\rm eff} = 3040$ K) and A. Gianninas et al. (2015; 0.27 $M_\odot$, $T_{\rm eff} = 3060$ K). However, given the poor quality of these fits, we do not consider these parameters to be reliable. Note also that the solution obtained using the M. Abel et al. (2012) grid exhibits similar issues to those encountered with WD J1922 +0233 for the same model grid: it severely underpredicts the flux in the optical region and predicts a strong absorption feature at 1.2 μm, in clear disagreement with the observations.

4.3. LHS 1126

Figure 8 presents our best-fit solutions to the JWST spectrum of LHS 1126. We also show its HST/FOS spectrum (B. Wolff et al. 2002), although it was not included in our fitting procedure to maintain consistency with our analysis of the two

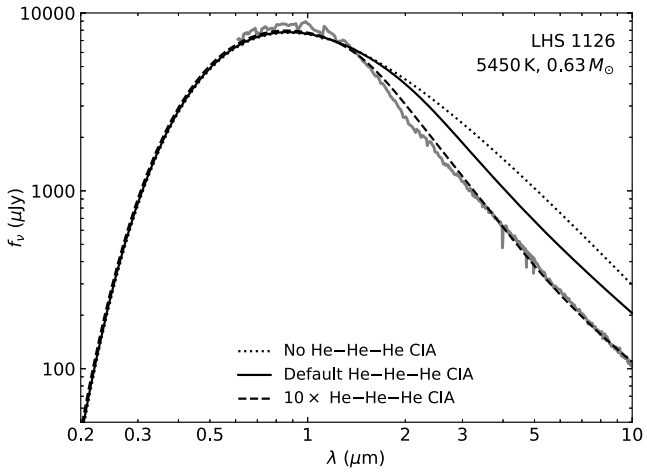

Figure 9. Model spectra for a helium-atmosphere white dwarf with the same parameters as the best-fit pure-helium solution shown in Figure 8. The solid line is the model obtained using the default He–He–He CIA of P. M. Kowalski (2014), as in the model shown as a dotted dark blue line in Figure 8. The dotted and dashed lines illustrate the effect of decreasing or increasing this absorption source. The JWST data are shown for comparison. This supports the idea that an enhanced He–He–He CIA could explain LHS 1126's SED.

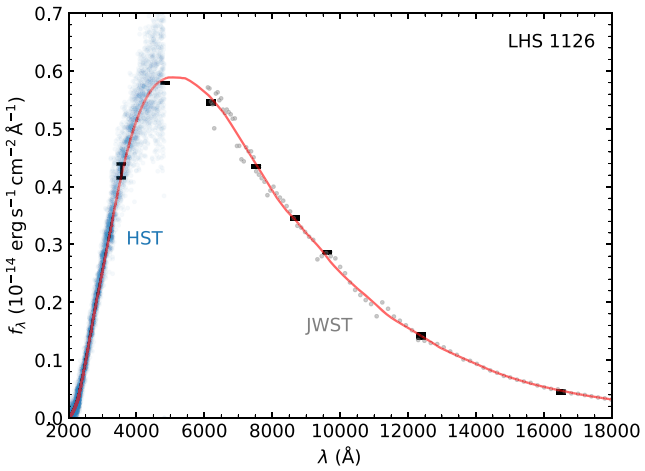

Figure 10. Smoothed SED (red curve) used to calculate the total wavelength-integrated flux of LHS 1126. The HST and JWST data points used to build the smoothed SED are shown as blue and gray symbols. Archival optical and infrared photometry is also shown with black error bars.

previous stars. Similar to LHS 3250, the fits are unsatisfactory due to the predicted 2.4 μm feature in the hydrogen–helium solutions, which is absent in the JWST data. While the fit in the visible range is good, the ultraviolet flux is severely underestimated due to the red wing of the Lyα line (see also S. Blouin et al. 2019b).

The complete absence of any feature (absorption or emission-like) at 2.4 μm strongly suggests a very low hydrogen abundance in LHS 1126's atmosphere. Given the precision of the JWST data, we found that any amount of hydrogen superior to $\log \mathrm{H/He} = -5$ would lead to a detectable absorption feature at 2.4 μm, a result that applies both with the M. Abel et al. (2012) and U. G. Jørgensen et al. (2000) grids. This is consistent with the presence of (very weak) C_2 Swan bands in its optical spectrum, as cool DQ white dwarfs are known to have very low levels of hydrogen in their atmospheres. This is evidenced by the near-universal absence of CH features in such stars (S. Blouin & P. Dufour 2019; S. Blouin et al. 2019b; M. Kilic et al. 2024, in preparation). Given these indications, we attempted to fit the full SED (taking into consideration both the HST and JWST data) using a hydrogen-free model atmosphere grid.[8] While the overall fit is reasonable, there is insufficient absorption in the infrared to match the JWST data, despite the inclusion of He–He–He CIA from P. M. Kowalski (2014) in our models. It is noteworthy that the three best-fit solutions shown in Figure 8 yield remarkably similar effective temperatures and masses.

The strength of He–He–He CIA is highly sensitive to density, scaling with the cube of the helium density. This implies that small adjustments to the nonideal helium ionization at high densities, which controls the atmospheric density and remains highly uncertain (P. M. Kowalski et al. 2007), could significantly enhance He–He–He CIA. Adjustments to the He^- free–free opacity could have a similar effect. Figure 9 illustrates how an enhanced He–He–He CIA could potentially explain the full SED of LHS 1126. Specifically, this figure demonstrates that a tenfold increase in He–He–He CIA would be sufficient to match the infrared flux level of LHS 1126, which corresponds to a density increase of only a factor of $\sim$2. Such a change in the density structure of pure-helium model atmospheres is well within the uncertainties of our current understanding of nonideal effects in high-density helium (D. Saumon et al. 2022).

Given the extensive flux-calibrated data for LHS 1126 covering essentially its entire SED, we can also establish constraints on its atmospheric parameters that are independent of model atmospheres. We first performed a simple smoothing of the available HST+JWST data with a Savitzky–Golay filter (Figure 10) to obtain a complete SED, which we then integrated. This integral is directly related to $T_{\rm eff}$ and the star's radius in a way that is completely independent of model atmospheres:

$$\int f_\lambda \, d\lambda = \sigma T_{\rm eff}^4 \frac{R^2}{D^2}, \tag{1}$$

where σ is the Stefan–Boltzmann constant. Using a standard mass–radius relation (A. Bédard et al. 2022) and the Gaia-based distance, we derived a well-defined relation for the possible mass–$T_{\rm eff}$ values of LHS 1126 (Figure 11). This figure shows that our pure-helium solution of Figure 8 perfectly matches the model-independent constraint. While this agreement is not surprising, given that we used the same HST and JWST data in our model fitting process, it is nonetheless a welcome reassurance considering the high uncertainties surrounding IR-faint models.

5. On the Origin of the Emission-like Features

We now explore possible causes for the emission-like feature at 2.4 μm detected in LHS 3250 and WD J1922+0233. We exclude LHS 1126 from this discussion, as the absence of any feature in its infrared spectrum (and therefore extremely low hydrogen abundance) places it in a distinct category from the other two IR-faint white dwarfs.

[8] The very small carbon trace ($\log \mathrm{C/He} = -8.4$; S. Blouin et al. 2019b) in LHS 1126's atmosphere can be neglected. At the cool effective temperatures relevant to our analysis, it has no effect on the shape of the optical and infrared SED. Pressure-ionized helium is by far the main free-electron contributor (see Figure 2 of S. Blouin et al. 2023a). This carbon abundance was also previously found to be too low to result in detectable C_2–He CIA (S. Blouin et al. 2019b). The impact of carbon is limited to weak Swan bands and atomic absorption blueward of 0.2 μm.

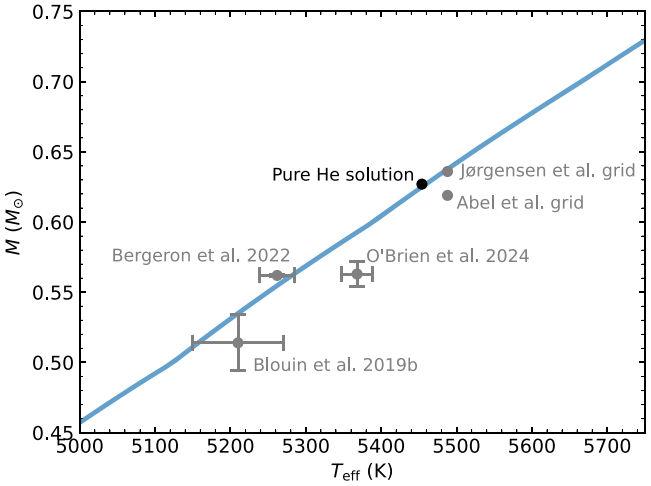

Figure 11. The blue line marks the combinations of masses and effective temperatures that are compatible with the parallax and wavelength-integrated flux of LHS 1126. We have estimated the uncertainty to be comparable to the width of this line. The pure-helium solution of Figure 8 is indicated with a black circle. Gray symbols also report other solutions published in the literature (S. Blouin et al. 2019b; P. Bergeron et al. 2022; M. W. O'Brien et al. 2024) as well as our mixed hydrogen–helium solutions (which we rejected).

5.1. Density Distortion Effects

Based on density functional theory molecular dynamics simulations, S. Blouin et al. (2017) predict that at densities above 0.1 g cm^{-3}, the 2.4 μm H_2–He CIA band can split into two components. The resulting CIA spectrum then exhibits a local minimum between two absorption peaks (Figure 12). At first glance, this effect appears similar to what we observe in the infrared spectrum of WD J1922+0233 (Figure 5), where the emission-like feature could be interpreted as the local minimum of the CIA spectrum.

However, there are significant problems with this interpretation. First, this effect is already included in our model grid, and yet it does not appear in our best-fit models. We also fail to see this effect in much cooler models (e.g., for the atmospheric parameters of WD J1922+0233 determined by A. K. Elms et al. 2022), as shown in Figure 12 of S. Blouin et al. (2017). This is primarily because in the CIA-forming regions of the atmosphere, which are well above the photosphere due to the strong opacity at wavelengths affected by CIA, the density is simply too low for these CIA distortion effects to significantly impact the emerging spectrum. One might argue that this could indicate that the density is severely underestimated in these cool hydrogen–helium models. However, there are already clear indications that the density might actually be overestimated. Using the same models as those used here, P. Bergeron et al. (2022) found it impossible to account for the narrowness of WD J1922+0233's Na absorption line (see their Figure 11). The predicted Na feature is much too wide, suggesting that the density in the line-forming region of the atmosphere is significantly lower than predicted by the models. A. K. Elms et al. (2022) encountered a similar problem and chose to arbitrarily reduce the broadening constant of the offending lines by a factor of 100.

A second issue is that this interpretation fails to explain the spectrum of LHS 3250. The density distortion effect only predicts a reduction in absorption at the center of the 2.4 μm band, not a complete elimination of absorption across the band or the presence of an emission-like feature. An absorption profile like that shown in Figure 12, even with significant distortion, would still result in net absorption across the entire band, which is inconsistent with the observations of LHS 3250. These issues strongly suggest that density distortion effects alone are insufficient to explain the observed spectral features in WD J1922+0233 and LHS 3250.

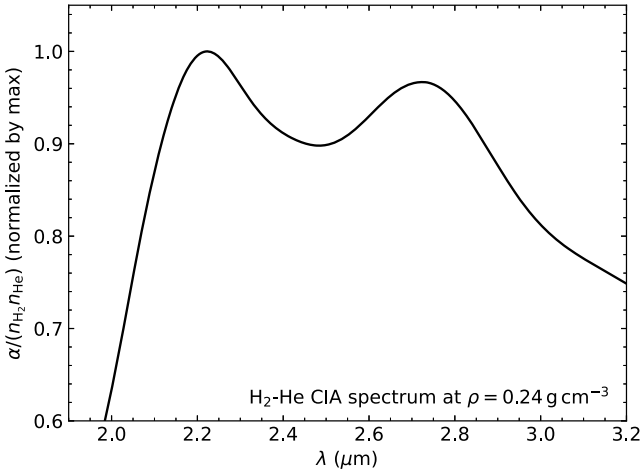

Figure 12. H_2–He CIA spectrum at $\rho = 0.24$ g cm^{-3} according to S. Blouin et al. (2017). Note the split of the 2.4 μm band. This particular spectrum was obtained at $T = 5000$ K.

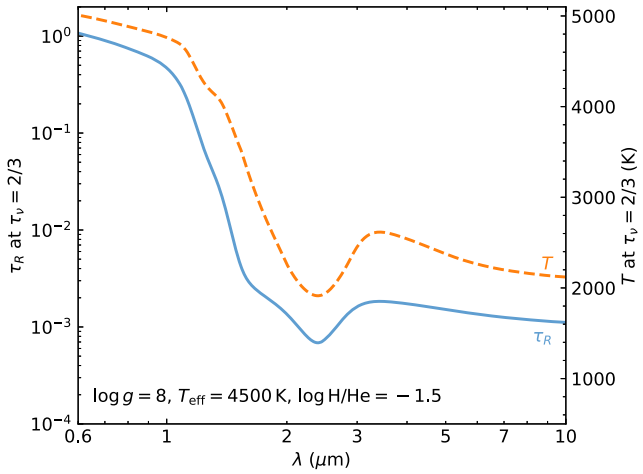

Figure 13. Rosseland mean optical depth at which $\tau_\nu = 2/3$ as a function of wavelength (solid line, left axis) and temperature at that same depth (dashed line, right axis). Note how the strong CIA opacity implies that the infrared portion of the spectrum is formed much higher in the atmosphere than the photosphere.

5.2. Temperature Inversion above the Photosphere

A temperature inversion in the upper atmosphere of WD J1922+0233 and LHS 3250 could potentially explain their emission-like feature. Due to the high opacity at CIA-forming wavelengths, we probe increasingly higher atmospheric layers as we approach peak-CIA absorption at 2.4 μm. Figure 13 illustrates this effect, showing in blue the Rosseland optical depth from which the typical photon emerges (i.e., where $\tau_\nu = 2/3$) for a model with parameters typical of hydrogen–helium-atmosphere IR-faint white dwarfs. At 2.4 μm, the typical photon emerges from a region where $\tau_R \lesssim 10^{-3}$, well above the photosphere (where $\tau_R = 2/3$ by definition). Under standard conditions, where temperature decreases from the photosphere outward, the temperature in this

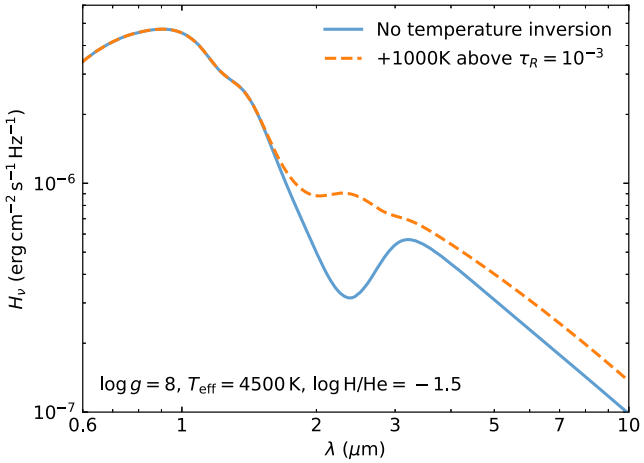

Figure 14. Model spectrum of an IR-faint white dwarf based on a thermodynamic structure found using the standard linearization technique to reach radiative equilibrium (solid line) and model spectrum for the same star but with an ad hoc 1000 K increase in the temperature profile above $\tau_R = 10^{-3}$ (dashed line).

region is lower than at the photosphere (dashed orange line in Figure 13). However, if the temperature happens to be higher in these upper atmospheric levels, the star could appear brighter at these wavelengths.

Figure 14 demonstrates this effect. We artificially increased the temperature of the uppermost layers ($\tau_R < 10^{-3}$) by 1000 K. This does not affect the flux below 1.5 μm, where the continuum forms deeper than $\tau_R = 10^{-3}$. However, it increases the flux where CIA is strong, particularly at its peak. This results in enhanced thermal emission at 2.4 μm, creating a small flux bump not too different to that observed in LHS 3250 (Figure 7). We stress that this 1000 K boost is entirely ad hoc, serving solely as a proof of concept. Possible explanations for such a temperature inversion are discussed in Section 5.3.

Reproducing the narrow emission-like feature seen in WD J1922+0233's spectrum with a temperature inversion has proved more challenging. A key difficulty is that increasing the temperature broadens the 2.4 μm feature (Figure 6), conflicting with the narrow feature observed in WD J1922+0233. Consequently, we could only obtain an emission-like feature at 2.4 μm resembling WD J1922+0233's spectrum by assuming a much lower $T_{\rm eff}$ than found in our earlier analysis (Figure 15). Reducing $T_{\rm eff}$ results in lower temperatures in the region above the photosphere, which in turn allows us to introduce a temperature inversion while still maintaining temperatures low enough to preserve a narrow CIA feature.

The temperature inversion hypothesis appears particularly promising for explaining the spectral features of LHS 3250, but presents more challenges when applied to WD 1922+0233 due to the narrowness of the observed emission-like feature. However, it would be premature to discard the temperature inversion idea for WD J1922+0233 based on this issue alone.

First, Occam's razor suggests we should prefer a common explanation for the emission-like features of both LHS 3250 and WD J1922+0233, rather than invoking separate mechanisms for each star.

Second, the opacity sources that shape the temperature structure of cool hydrogen–helium IR-faint white dwarf atmospheres (Figure 16) are notoriously uncertain (R. S. McWilliams et al. 2015; D. Saumon et al. 2022). The low-mass problem identified in

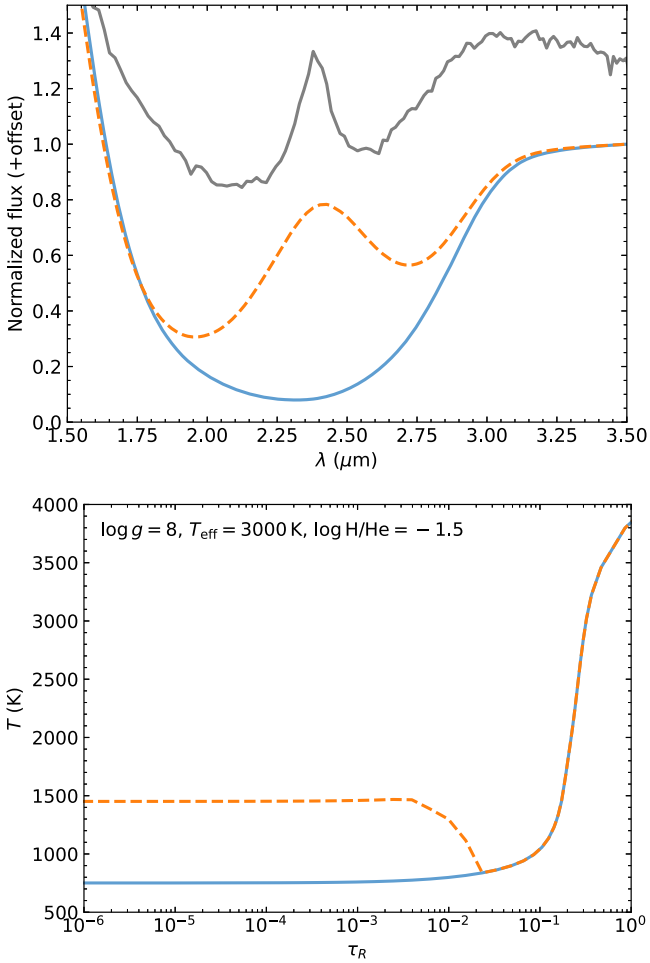

Figure 15. Top: JWST spectrum of WD J1922+0233 (gray) in the H_2 fundamental band region, compared to a standard ultracool model ($T_{\rm eff}$ = 3000 K, log H/He = −1.5; blue solid line) and the same model with an ad hoc temperature inversion in the upper atmosphere (orange dashed line). All three spectra were normalized at 3.5 μm, and the JWST spectrum was vertically shifted for clarity. Bottom: temperature structures underlying the two model spectra shown in the top panel.

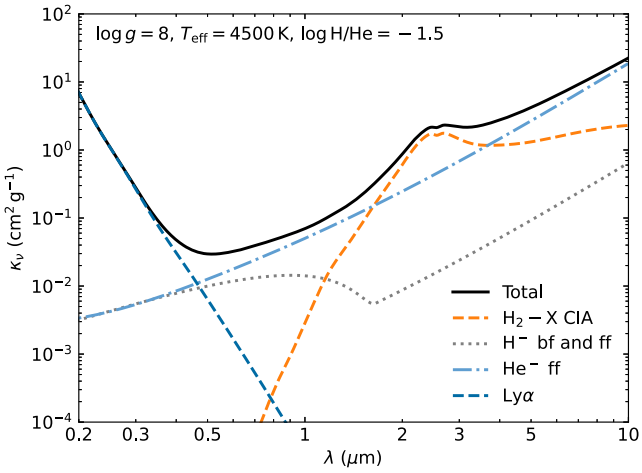

Figure 16. Main contributions to the total opacity at the photosphere (τ_R = 2/3) of a typical IR-faint white dwarf. Note the small split in the 2.4 μm CIA band opacity. Consistent with our discussion in Section 5.1, this split is far too weak to significantly affect the emerging spectrum.

the Gaia data for cool white dwarfs probably points to significant problems with opacities for pure-hydrogen atmospheres at low temperatures (A. Caron et al. 2023; M. W. O'Brien et al. 2024). These issues are likely exacerbated in hydrogen–helium atmospheres due to their higher densities and more complex opacity physics. For a model with $T_{\rm eff} = 4500$ K, $\log g = 8$, and $\log {\rm H/He} = -1.5$, we find that changing the He^- free–free opacity or the H^- opacities by a factor of 10 results in a 1000 K change in the temperature at $\tau_R = 10^{-3}$. In addition, three-dimensional simulations of pure-hydrogen atmospheres have revealed a significant reduction of the temperature in the uppermost layers due to overshooting motions that force the entropy gradient in the stable layers above the convection zone to approach a near-adiabatic structure (P. E. Tremblay et al. 2013). Naturally, a similar effect can be expected to impact hydrogen–helium atmospheres. For these reasons, the temperature in the uppermost layers of our IR-faint model atmospheres may be overestimated by a nonnegligible margin. This would in turn allow for a more significant temperature inversion without reaching temperatures that would overly broaden the CIA features.

Third, non–local thermodynamic equilibrium (non-LTE) effects in the uppermost region of the atmosphere cannot be ruled out. The models used in this work assume LTE, and a definitive assessment of non-LTE effects would require calculations using a non-LTE atmosphere code that incorporates all relevant microphysics for cool hydrogen–helium-atmosphere white dwarfs. Such a code is not currently available. If present, non-LTE effects could potentially result in H_2–He collision-induced emission (L. Frommhold 1993), which might contribute to the narrow feature observed in WD J1922+0233 at 2.4 μm.

Finally, as discussed above, WD J1922+0233 also displays a surprisingly narrow Na line (P. Bergeron et al. 2022; A. K. Elms et al. 2022). This narrow feature is particularly perplexing when compared to other very cool DZ stars, which typically show very broad Na features that are satisfactorily reproduced by existing models (S. Blouin et al. 2019b; B. C. Kaiser et al. 2021). The fact that a star with ostensibly similar parameters behaves so differently cannot be easily explained by systematic problems with the model atmospheres' microphysics, as these would affect all cool DZ stars similarly. This suggests that the peculiarity must be more specific to WD J1922+0233 itself. In this context, invoking a peculiar temperature stratification for WD J1922+0233 becomes more plausible.

Given these considerations, while challenges remain in fully explaining the narrow emission-like feature in WD J1922+0233, we view the temperature inversion hypothesis as a promising avenue for understanding the infrared spectra of both LHS 3250 and WD J1922+0233.

5.3. Possible Causes of the Temperature Inversion

If a temperature inversion in the upper atmosphere is indeed responsible for the emission-like features observed in LHS 3250 and WD J1922+0233, then what is causing it? We explore two main scenarios.

One potential explanation draws parallels with DAe white dwarfs, which exhibit Balmer lines in absorption with emission cores at their centers (A. K. Elms et al. 2023). These objects are thought to be related to the more numerous DAHe white dwarfs, where Zeeman splitting is also detected (J. L. Greenstein & J. K. McCarthy 1985; C. J. Manser et al. 2023). The spectral features of DA(H)e stars are likely explained by an intrinsic temperature inversion (chromosphere) supported by the white dwarf's magnetic field (N. Walters et al. 2021; A. F. Lanza et al. 2024). A similar mechanism could be at work in IR-faint white dwarfs, with the emission-like feature in the H_2–He CIA band analogous to the Balmer line emission cores in DA(H)e stars. This scenario would require the presence of a magnetic field in LHS 3250 and WD J1922+0233. While no magnetic field has been detected in these objects, DAe white dwarfs also lack detectable fields, yet one is likely required to explain their emission features.

Recent evidence suggests an increased occurrence of magnetic fields in cool white dwarfs (S. Bagnulo & J. D. Landstreet 2022), although the picture below $T_{\rm eff} = 5000$ K is less clear due to the need for spectropolarimetry to detect magnetic fields in the absence of Balmer lines (A. V. Berdyugin et al. 2022; A. Berdyugin et al. 2024). It is thus a priori plausible that a significant fraction of IR-faint white dwarfs possess magnetic fields strong enough to support a chromosphere. H. C. Harris et al. (1999) presented spectropolarimetry of LHS 3250 and did not detect a magnetic field, but it is still unclear how strong the field needs to be to create a temperature inversion.

To further investigate this scenario, we searched for photometric variability in LHS 3250 and WD J1922+0233, as most DA(H)e white dwarfs are known to be variable (A. K. Elms et al. 2023). Analysis of TESS data for LHS 3250 (including both 20 s and 2 minutes cadence observations from several sectors) revealed no significant photometric variations. For WD J1922+0233, we acquired high-speed photometry of WD J1922+0233 on UT 2024 June 6 using the Apache Point Observatory (APO) 3.5 m telescope with the ARCTIC imager and the BG40 filter. We obtained back-to-back exposures of 25.5 s over 207 minutes under clear skies and 1.″0 seeing. To reduce the read-out time, we binned the CCD by 3×3, which resulted in a plate scale of 0.″34 pixel^{-1}. This setup has a read-out time of 4.5 s, which results in a cadence of $\approx$30 s in our light curves. As with LHS 3250, we find no evidence of variability (Figure 17) and therefore no additional supporting evidence for this scenario.

An alternative explanation is that temperature inversions occur naturally in the atmospheres of these stars, without any additional heating source. Such inversions can arise in LTE model atmospheres when a change in the dominant absorbing species induces a change in the frequency dependence of the absorption (S. Dumont & N. Heidmann 1973). A temperature inversion can then become necessary to satisfy the radiative equilibrium condition. This phenomenon has been observed in some white dwarfs (e.g., B. Klein et al. 2020) and has been reported for cool white dwarf model atmospheres due to the competition between H^- and CIA opacities (D. Saumon et al. 1994; P. Bergeron et al. 1995).

While our default models of IR-faint white dwarfs do not show the sort of temperature inversions that could explain the observed emission-like features of LHS 3250 and WD J1922+0233, this does not necessarily rule out this mechanism. The temperature structure in the upper atmosphere is extremely sensitive to the details of different opacity sources, which remain uncertain for these objects (as discussed in Section 5.2). Improvements in our treatment of opacities could potentially lead to models that naturally produce temperature inversions. To illustrate the sensitivity of the temperature structure in the upper layers to small perturbations, Figure 18 demonstrates

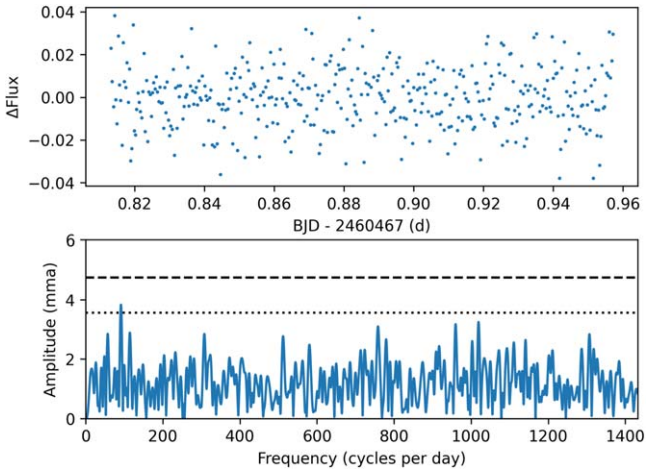

Figure 17. High-speed photometry of WD J1922+0233 obtained with the APO 3.5 m telescope. The top panel shows the light curve, and the bottom panel displays its Fourier transform plotted up to the Nyquist frequency. The dotted and dashed lines show the $3\langle A\rangle$ and $4\langle A\rangle$ levels (3.6 and 4.7 mma, respectively), where $\langle A\rangle$ is the average amplitude in the Fourier transform. There is no evidence of any significant photometric variability in the APO data for WD J1922+0233.

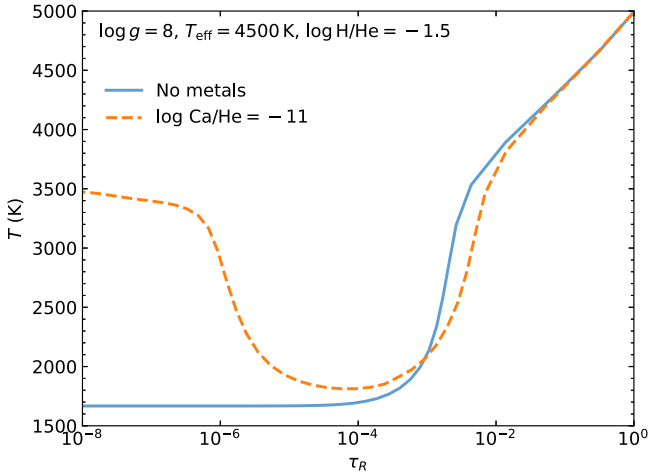

Figure 18. Thermal structures of IR-faint model atmospheres at 4500 K with and without metals. The addition of metals changes the opacity in a way that induces a temperature inversion in the upper atmosphere, while not affecting the photospheric conditions.

how adding a trace amount of metals to the atmosphere of an IR-faint white dwarf is enough to induce a strong temperature inversion. Note however that in this particular case the inversion happens too high above the photosphere to create an emission-like feature in the infrared spectrum. We saw in Figure 13 that for a star with these atmospheric parameters, the 2.4 μm CIA feature is mostly formed at $\tau_R \sim 10^{-3}$.

A related possibility is that a temperature inversion could be induced by a stratification in the composition of the star's atmosphere (P. M. Manseau et al. 2016). In a stratified atmosphere, the hydrogen abundance would be higher in the upper layers due to gravitational settling. However, this seems unlikely for an IR-faint white dwarf. At $T_{\rm eff} = 4500$ K, $\log g = 8$, and $\log {\rm H/He} = -1.5$, the atmosphere is convective below $\tau_R \simeq 10^{-3}$ and hence completely mixed in that region. One might think that an unmixed chemical stratification is possible above the convective boundary, but overshooting convective plumes should rapidly mix this region as well (P. E. Tremblay et al. 2013). This scenario therefore appears to be ruled out.

6. Keck NIRES Spectroscopy

As a complement to our JWST observations, we obtained near-infrared spectroscopy of seven IR-faint white dwarfs with the Near-Infrared Echellette Spectrometer (NIRES; J. C. Wilson et al. 2004) mounted on the Keck II telescope on UT 2023 September 26. The observed targets were WD J002702.93+055433.39, WD J080440.63+223949.68, WD J172257.78+575250.53, WD J195151.76+402629.07, WD J215008.33−043900.36, WD J224206.18+004822.94, and WD J230550.09+392232.87, all known IR-faint white dwarfs (P. Bergeron et al. 2022). NIRES provides $R = 2700$ spectra over five cross-dispersed orders covering the wavelength range of 0.9–2.45 μm. We obtained 5 minutes long exposures in an ABBA dither pattern along the slit, which was aligned with the parallactic angle. We repeated the observing sequence 3–4 times for each star, resulting in 12 or 16 spectra, and a total on-source integration time of 60 or 80 minutes. The spectra were extracted using a modified version of the SpeXTool package (W. D. Vacca et al. 2003; M. C. Cushing et al. 2004), with nearby A0 V stars used for telluric correction.

While the noise level of the NIRES spectra is too high to draw conclusions about the peak-CIA region near 2.4 μm, they provide valuable information at shorter wavelengths. Our JWST observations of WD J1922+0233 and LHS 3250 revealed the absence of a 1.2 μm feature, which we interpreted as evidence against ultracool temperatures for these objects. The Keck NIRES spectra offer an opportunity to test whether this conclusion extends to a larger sample of IR-faint white dwarfs.

Figure 19 presents the Keck NIRES spectra for our seven additional targets (left panel), along with model predictions for various effective temperatures (right panel). The observed spectra are not compatible with the pronounced 1.2 μm features predicted by model atmospheres for ultracool effective temperatures of 4000 K or below, regardless of whether we use the U. G. Jørgensen et al. (2000) or the M. Abel et al. (2012) CIA opacities (the exact wavelength of the feature differs between both grids of models). This conclusion holds true regardless of the assumed hydrogen abundance, provided it is sufficient to produce significant H_2–He CIA. These results further corroborate the "not-so-cool" hypothesis of P. Bergeron et al. (2022), extending the conclusions drawn from our JWST observations to a broader sample.

7. Discussion and Conclusions

We have presented JWST spectra of three IR-faint white dwarfs, resolving for the first time the precise shape of CIA in those objects. While by far the most striking finding is the emission-like feature detected in the spectrum of WD J1922+0233, we have seen that the absence of features can sometimes be equally informative. In this last section, we discuss the implications of our findings for each object and outline directions for future research.

LHS 1126 appears to be a distinct case within the IR-faint population. We found that its infrared flux depletion is most likely caused by He–He–He CIA as we do not detect any feature in its JWST spectrum that can be associated with molecular hydrogen. We placed an upper limit of $\log {\rm H/He} = -5$ on its photospheric

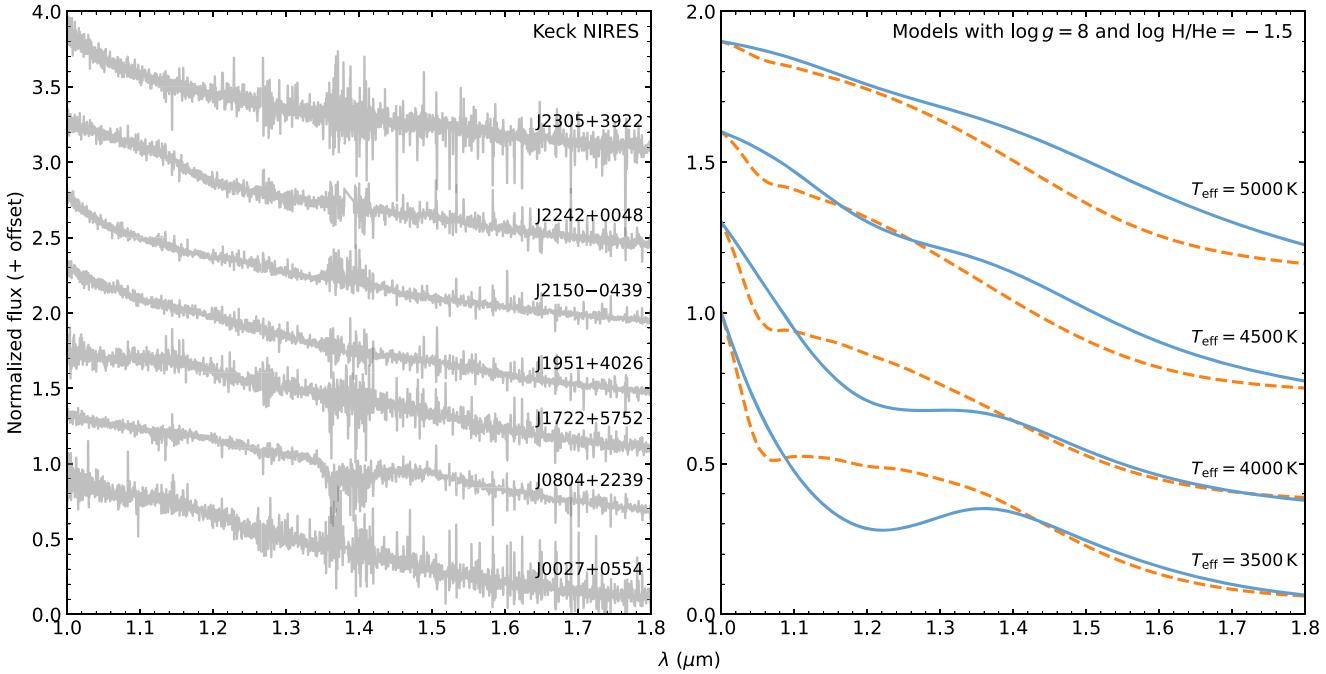

Figure 19. Left: Keck NIRES spectra of seven IR-faint white dwarfs. The spectra are normalized and vertically offset for clarity. Right: model spectra for white dwarfs with $\log g = 8$ and $\log{\rm H/He} = -1.5$ at various effective temperatures. Solid blue lines represent models using the M. Abel et al. (2012) H_2–He CIA opacities, while dashed orange lines show models using the U. G. Jørgensen et al. (2000) opacities. Note the absence of a pronounced molecular hydrogen first overtone band near 1.2 μm in the observed spectra.

hydrogen abundance, which implies a hydrogen content smaller than 10^{-10} of its total mass (B. Rolland et al. 2018). However, current models appear to be underestimating He–He–He CIA by a factor of ∼10, possibly due to uncertainties in the CIA calculations or inaccuracies in the density structure of pure-helium-atmosphere models. We derived a mass of 0.63 $M_\odot$ for LHS 1126, which is higher than the typical ≃0.55 $M_\odot$ found for cool DQs (S. Coutu et al. 2019; D. Koester & S. O. Kepler 2019; A. Caron et al. 2023). This is perfectly consistent with the fact that LHS 1126 exhibits unusually weak Swan bands for a DQ white dwarf at its temperature. Indeed, evolutionary models predict that more massive white dwarfs dredge up less carbon from their interiors (A. Bédard et al. 2022). Finding a higher-than-average mass for a DQ white dwarf with weak carbon features aligns well with these predictions.

For LHS 3250 and WD J1922+0233, the presence of features at 2.4 μm, coinciding with peak H_2–He CIA absorption, indicates the presence of hydrogen in their atmospheres. While not explicitly discussed earlier, we have ruled out pure-hydrogen atmospheres in favor of mixed hydrogen–helium compositions. This is supported by better overall SED fits with mixed models and the stars' position in a sparsely populated region of the color–magnitude diagram (Figure 1). Since it is expected that even at cool temperatures most white dwarfs have hydrogen-dominated atmospheres, hydrogen-atmosphere white dwarfs must be populating a more crowded region of the color–magnitude diagram (i.e., the cool end of the A/B branch in Figure 1). The location of LHS 3250 and WD J1922+0233 in the less populated IR-faint region thus indicates a mixed composition. These objects likely followed the evolutionary pathway described by P. Bergeron et al. (2022), where a deepening hydrogen convection zone transforms pure-hydrogen atmospheres into mixed hydrogen–helium atmospheres at lower temperatures.

The absence of a 1.2 μm CIA feature in the JWST spectra of LHS 3250 and WD J1922+0233 (and the lack of a pronounced 1.2 μm feature in the Keck NIRES spectra of seven additional IR-faint white dwarfs) argues against ultracool temperatures, consistent with the conclusions of P. Bergeron et al. (2022). Our analysis also yields relatively high masses for these two stars. A previously unmentioned benefit of these high masses is that they could naturally explain the extreme rarity of metal pollution in IR-faint white dwarfs, with just one out of 37 (P. Bergeron et al. 2022) compared to ∼30% of helium-atmosphere white dwarfs in the 4000–5000 K range. This is because massive white dwarfs are generally much less likely to be metal polluted (D. Koester et al. 2014). However, the narrowness of WD J1922+0233's Na absorption line in the optical remains unexplained.

The fact that we observe an emission-like feature at 2.4 μm in two out of two IR-faint white dwarfs with hydrogen–helium atmospheres suggests that such features may be ubiquitous in this population. This previously unrecognized phenomenon may explain the persistent difficulties in fitting IR-faint white dwarf SEDs over the past 25 yr. Our analysis suggests that the emission-like features observed in IR-faint white dwarfs could be explained by a temperature inversion above the photosphere. However, without a good predictive model to explain this behavior, the precise parameters of IR-faint white dwarfs remain uncertain. Unlike most stellar atmospheres where upper atmospheric effects primarily influence spectral line cores, the situation is different for IR-faint white dwarfs, since the infrared continuum is strongly affected by the CIA acting well above the photosphere. This implies that even photometric fits are sensitive to these temperature inversions. Until we develop an understanding of the mechanisms causing this temperature inversion and incorporate it into our models, precise

characterization of IR-faint white dwarfs with mixed atmospheres will remain challenging.

We end by highlighting several research directions that could help further elucidate the nature of IR-faint white dwarfs. First, spectropolarimetric observations of additional IR-faint white dwarfs could reveal magnetic fields, thereby testing the idea that these white dwarfs host magnetic fields that support a chromosphere responsible for the observed emission-like features. Second, theoretical and laboratory studies of He^- free–free absorption, H^- bound-free absorption, Lyα broadening, and CIA under conditions relevant to cool white dwarf atmospheres would improve our understanding of these objects and cool white dwarfs in general. Last but not least, additional JWST observations of IR-faint white dwarfs are crucial to determine whether the 2.4 μm emission-like feature is ubiquitous in this population. The diverse spectra observed in the three stars studied here further underscore the need for additional observations. Each object presents unique characteristics, suggesting that a larger sample may reveal even more unexpected features.

Acknowledgments

S.B. thanks Pierre Bergeron for insightful discussions on model atmospheres and René Doyon for encouraging the application for time to observe IR-faint white dwarfs with JWST. The authors thank the anonymous referee for their useful comments. S.B. acknowledges the support of the Canadian Space Agency (CSA; 23JWGO2A10) and of the Canadian Institute for Theoretical Astrophysics (CITA). M.K. acknowledges support by the NSF under grant AST-2205736 and NASA under grant Nos. 80NSSC22K0479, 80NSSC24K0380, and 80NSSC24K0436.

This work is based on observations made with the NASA/ESA/CSA James Webb Space Telescope. The data were obtained from the Mikulski Archive for Space Telescopes at the Space Telescope Science Institute, which is operated by the Association of Universities for Research in Astronomy, Inc., under NASA contract NAS 5-03127 for JWST. These observations are associated with program #3168. Support for this program was provided through a grant from the STScI under NASA contract NAS 5-03127.

The Apache Point Observatory 3.5 m telescope is owned and operated by the Astrophysical Research Consortium.

This work was supported by a NASA Keck PI Data Award, administered by the NASA Exoplanet Science Institute. Data presented herein were obtained at the W.M. Keck Observatory from telescope time allocated to the National Aeronautics and Space Administration through the agency's scientific partnership with the California Institute of Technology and the University of California. The Observatory was made possible by the generous financial support of the W. M. Keck Foundation.

The authors wish to recognize and acknowledge the very significant cultural role and reverence that the summit of Maunakea has always had within the indigenous Hawaiian community. We are most fortunate to have the opportunity to conduct observations from this mountain.

This work has made use of data from the European Space Agency (ESA) mission Gaia (https://www.cosmos.esa.int/gaia), processed by the Gaia Data Processing and Analysis Consortium (DPAC, https://www.cosmos.esa.int/web/gaia/dpac/consortium). Funding for the DPAC has been provided by national institutions, in particular the institutions participating in the Gaia Multilateral Agreement.

This work has made use of the Montreal White Dwarf Database (P. Dufour et al. 2017).

ORCID iDs

Simon Blouin https://orcid.org/0000-0002-9632-1436
Mukremin Kilic https://orcid.org/0000-0001-6098-2235
Loïc Albert https://orcid.org/0000-0003-0475-9375
Bianca Azartash-Namin https://orcid.org/0000-0002-7898-6194
Patrick Dufour https://orcid.org/0000-0003-4609-4500

References

Abel, M., Frommhold, L., Li, X., & Hunt, K. L. C. 2012, JChPh, 136, 044319
Bagnulo, S., & Landstreet, J. D. 2022, ApJL, 935, L12
Becker, A., Lorenzen, W., Fortney, J. J., et al. 2014, ApJS, 215, 21
Bédard, A., Blouin, S., & Cheng, S. 2024, Natur, 627, 286
Bédard, A., Brassard, P., Bergeron, P., & Blouin, S. 2022, ApJ, 927, 128
Berdyugin, A., Landstreet, J. D., Bagnulo, S., Piirola, V., & Berdyugina, S. V. 2024, A&A, 690, A10
Berdyugin, A. V., Piirola, V., Bagnulo, S., Landstreet, J. D., & Berdyugina, S. V. 2022, A&A, 657, A105
Bergeron, P., Dufour, P., Fontaine, G., et al. 2019, ApJ, 876, 67
Bergeron, P., Kilic, M., Blouin, S., et al. 2022, ApJ, 934, 36
Bergeron, P., & Leggett, S. K. 2002, ApJ, 580, 1070
Bergeron, P., Leggett, S. K., & Ruiz, M. T. 2001, ApJS, 133, 413
Bergeron, P., Saumon, D., & Wesemael, F. 1995, ApJ, 443, 764
Blouin, S., Bédard, A., & Tremblay, P.-E. 2023a, MNRAS, 523, 3363
Blouin, S., Daligault, J., & Saumon, D. 2021, ApJL, 911, L5
Blouin, S., & Dufour, P. 2019, MNRAS, 490, 4166
Blouin, S., Dufour, P., & Allard, N. F. 2018a, ApJ, 863, 184
Blouin, S., Dufour, P., Allard, N. F., & Kilic, M. 2018b, ApJ, 867, 161
Blouin, S., Dufour, P., Allard, N. F., et al. 2019a, ApJ, 872, 188
Blouin, S., Dufour, P., Thibeault, C., & Allard, N. F. 2019b, ApJ, 878, 63
Blouin, S., Kilic, M., Bédard, A., & Tremblay, P.-E. 2023b, MNRAS, 525, L112
Blouin, S., Kowalski, P. M., & Dufour, P. 2017, ApJ, 848, 36
Borysow, A., Frommhold, L., & Moraldi, M. 1989, ApJ, 336, 495
Borysow, A., Jørgensen, U. G., & Fu, Y. 2001, JQSRT, 68, 235
Borysow, A., Jorgensen, U. G., & Zheng, C. 1997, A&A, 324, 185
Brown, W. R., Kilic, M., Allende Prieto, C., & Kenyon, S. J. 2010, ApJ, 723, 1072
Bushouse, H., Eisenhamer, J., Dencheva, N., et al. 2022, JWST Calibration Pipeline, v1.8.1, Zenodo, doi:10.5281/zenodo.7215690
Camisassa, M., Torres, S., Hollands, M., et al. 2023, A&A, 674, A213
Caron, A., Bergeron, P., Blouin, S., & Leggett, S. K. 2023, MNRAS, 519, 4529
Chambers, K. C., Magnier, E. A., Metcalfe, N., et al. 2016, arXiv:1612.05560
Coutu, S., Dufour, P., Bergeron, P., et al. 2019, ApJ, 885, 74
Cushing, M. C., Vacca, W. D., & Rayner, J. T. 2004, PASP, 116, 362
Dufour, P., Blouin, S., Coutu, S., et al. 2017, in ASP Conf. Ser. 509, 20th European White Dwarf Workshop, ed. P. E. Tremblay, B. Gaensicke, & T. Marsh (San Francisco, CA: ASP), 3, arXiv:1610.00986
Dumont, S., & Heidmann, N. 1973, A&A, 27, 273
Elms, A. K., Tremblay, P.-E., Gänsicke, B. T., et al. 2022, MNRAS, 517, 4557
Elms, A. K., Tremblay, P.-E., Gänsicke, B. T., et al. 2023, MNRAS, 524, 4996
Farihi, J. 2016, NewAR, 71, 9
Fontaine, G., Brassard, P., & Bergeron, P. 2001, PASP, 113, 409
Frommhold, L. 1993, Collision-induced Absorption in Gases, Cambridge Monographs on Atomic, Molecular, and Chemical Physics (Cambridge Univ. Press: Cambridge), 2
Gaia Collaboration, Prusti, T., de Bruijne, J. H. J., et al. 2016, A&A, 595, A1
Gaia Collaboration, Vallenari, A., Brown, A. G. A., et al. 2023, A&A, 674, A1
Gates, E., Gyuk, G., Harris, H. C., et al. 2004, ApJL, 612, L129
Gianninas, A., Curd, B., Thorstensen, J. R., et al. 2015, MNRAS, 449, 3966
Greenstein, J. L., & McCarthy, J. K. 1985, ApJ, 289, 732
Hansen, B. M. S. 1998, Natur, 394, 860
Hare, W. F. J., & Welsh, H. L. 1958, CaJPh, 36, 88
Harris, H. C., Dahn, C. C., Vrba, F. J., et al. 1999, ApJ, 524, 1000
Hollands, M. A., Tremblay, P.-E., Gänsicke, B. T., Koester, D., & Gentile-Fusillo, N. P. 2021, NatAs, 5, 451

Iglesias, C. A., Rogers, F. J., & Saumon, D. 2002, ApJL, 569, L111
Jakobsen, P., Ferruit, P., Alves de Oliveira, C., et al. 2022, A&A, 661, A80
Jørgensen, U. G., Hammer, D., Borysow, A., & Falkesgaard, J. 2000, A&A, 361, 283
Jura, M., Farihi, J., & Zuckerman, B. 2009, AJ, 137, 3191
Kaiser, B. C., Clemens, J. C., Blouin, S., et al. 2021, Sci, 371, 168
Kilic, M., Bergeron, P., Kosakowski, A., et al. 2020, ApJ, 898, 84
Kilic, M., Kowalski, P. M., Reach, W. T., & von Hippel, T. 2009, ApJ, 696, 2094
Kilic, M., von Hippel, T., Mullally, F., et al. 2006, ApJ, 642, 1051
Klein, B., Blouin, S., Romani, D., et al. 2020, ApJ, 900, 2
Koester, D., Gänsicke, B. T., & Farihi, J. 2014, A&A, 566, A34
Koester, D., & Kepler, S. O. 2019, A&A, 628, A102
Kowalski, P. 2006, PhD thesis, Vanderbilt Univ., Tennessee
Kowalski, P. M. 2010, A&A, 519, L8
Kowalski, P. M. 2014, A&A, 566, L8
Kowalski, P. M., Mazevet, S., Saumon, D., & Challacombe, M. 2007, PhRvB, 76, 075112
Lanza, A. F., Rui, N. Z., Farihi, J., Landstreet, J. D., & Bagnulo, S. 2024, A&A, 689, A233
Linsky, J. L. 1969, ApJ, 156, 989
Manseau, P. M., Bergeron, P., & Green, E. M. 2016, ApJ, 833, 127
Manser, C. J., Gänsicke, B. T., Inight, K., et al. 2023, MNRAS, 521, 4976
McWilliams, R. S., Dalton, D. A., Konôpková, Z., Mahmood, M. F., & Goncharov, A. F. 2015, PNAS, 112, 7925
O'Brien, M. W., Tremblay, P. E., Klein, B. L., et al. 2024, MNRAS, 527, 8687
Reach, W. T., Kuchner, M. J., von Hippel, T., et al. 2005, ApJL, 635, L161
Reach, W. T., Lisse, C., von Hippel, T., & Mullally, F. 2009, ApJ, 693, 697
Rieke, G. H., Ressler, M. E., Morrison, J. E., et al. 2015, PASP, 127, 665
Rolland, B., Bergeron, P., & Fontaine, G. 2018, ApJ, 857, 56
Saumon, D., Bergeron, P., Lunine, J. I., Hubbard, W. B., & Burrows, A. 1994, ApJ, 424, 333
Saumon, D., Blouin, S., & Tremblay, P.-E. 2022, PhR, 988, 1
Skrutskie, M. F., Cutri, R. M., Stiening, R., et al. 2006, AJ, 131, 1163
Swan, A., Farihi, J., Su, K. Y. L., & Desch, S. J. 2024, MNRAS, 529, L41
Tremblay, P. E., Ludwig, H. G., Steffen, M., & Freytag, B. 2013, A&A, 552, A13
Tremblay, P.-E., Fontaine, G., Gentile Fusillo, N. P., et al. 2019, Natur, 565, 202
Tremblay, P. E., Hollands, M. A., Gentile Fusillo, N. P., et al. 2020, MNRAS, 497, 130
Vacca, W. D., Cushing, M. C., & Rayner, J. T. 2003, PASP, 115, 389
Walters, N., Farihi, J., Marsh, T. R., et al. 2021, MNRAS, 503, 3743
Wilson, J. C., Henderson, C. P., Herter, T. L., et al. 2004, Proc. SPIE, 5492, 1295
Wolff, B., Koester, D., & Liebert, J. 2002, A&A, 385, 995